Chinese Chemical Letters 31 (2020) 2254–2258

Contents lists available at ScienceDirect

Chinese Chemical Letters

journal homepage: www.elsevier.com/locate/cclet

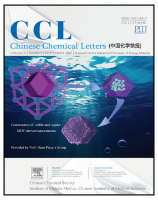

Communication

In-situ growth of hybrid $NaTi_8O_{13}/NaTiO_2$ nanoribbons on layered MXene Ti_3C_2 as a competitive anode for high-performance sodium-ion batteries

Xuan Sun[1], Ke Tan[1], Yang Liu, Jinyang Zhang, Linrui Hou*, Changzhou Yuan*

School of Material Science & Engineering, University of Jinan, Ji'nan 250022, China

ARTICLE INFO

Article history:
Received 2 January 2020
Received in revised form 27 January 2020
Accepted 11 February 2020
Available online 12 February 2020

Keywords:
Sodium titanate nanoribbons
Layered MXene Ti_3C_2
In-situ growth
Anodes
Sodium ion batteries

ABSTRACT

In the work, we successfully explore a two-step hydrothermal method for scalable synthesis of the hybrid sodium titanate ($NaTi_8O_{13}/NaTiO_2$) nanoribbons well *in-situ* formed on the multi-layered MXene Ti_3C_2 (designed as NTO/Ti_3C_2). Benefiting from the inherent structural and componential superiorities, the resulted NTO/Ti_3C_2 composite exhibits long-duration cycling stability and superior rate behaviors when evaluated as a hybrid anode for advanced SIBs, which delivers a reversible and stable capacity of ~82 mAh/g even after 1900 cycles at 2000 mA/g for SIBs.

It is common knowledge that rechargeable lithium-ion batteries (LIBs), one of the most important energy carriers, have been widely used in our daily life. However, the further and large-scale applications of LIBs are hindered by shortage of lithium resources, high production coast, and inherent safety problems. In this regard, more and more researchers have made an effort to develop other rechargeable metal-ion batteries [1–3]. Benefitting from the abundant reserves and low cost of sodium sources, sodium-ion batteries (SIBs) have promising applications in energy storage [4–6]. Similar to LIBs, the electrochemical behaviors of SIBs are highly dependent on the properties of the electrode materials. Unfortunately, due to the larger ionic radius of Na^+ (1.06 Å) in comparison with Li^+ (0.76 Å) [7,8], most of the anode materials suitable for LIBs cannot be directly used by SIBs, which will cause severe losses in energy capacity and cycle stability.

To date, many works focus on developing suitable anode candidates for SIBs, such as metal oxides/sulfides [9,10], porous carbon materials [11,12], metallic alloys [13,14]. Besides, previous studies showed that sodium titanate compounds ($Na_xTi_yO_z$) could be deemed as a promising class of SIB anode materials due to their high theoretical specific capacity of 178 mAh/g and lowest charge/discharge voltage plateau of 0.3 V *vs.* Na^+/Na [15,16]. Up to now, various smart nanostructured $Na_xTi_yO_z$ such as nanowires [17,18], nanosheets (NSs) [19], nanorods [20], were fabricated for shortening the Na^+-diffusion distance and increasing reaction interfaces. For example, recently, using $Ti_3C_2T_x$ (T for F, OH and O) as titanium source, Dong *et al.* prepared Ti_3C_2 MXene-derived $NaTi_{1.5}O_{8.3}$ nanoribbons by a simultaneous oxidation and alkalization processes, which offered an enhanced reversible capacity [21]. Unfortunately, the synthetic method in this work destroyed the texture of MXene entirely, which make the intrinsic advantages of the $Ti_3C_2T_x$ MXene cannot be utilized. As is known to all, the $Ti_3C_2T_x$ material could be an excellent natural matrix candidate in energy storage materials if two-dimensional (2D) robust structure, high conductivity and unique electronic properties of $Ti_3C_2T_x$ MXene could be fully utilized and synergistically interplayed with excellent components [22–27]. Besides, the inherent poor electrical conductivity and instable structure of $Na_xTi_yO_z$, which can cause sluggish kinetics and large capacity decay during cycle process thus poor electrochemical performance, can be addressed if the merits of $Ti_3C_2T_x$ were preserved.

Herein, the ultrathin $NaTi_8O_{13}/NaTiO_2$ (NTO) nanoribbons were *in-situ* grew on the multi-layered Ti_3C_2 surfaces through a facile yet effective two-step mild hydrothermal method, where the $Ti_3C_2T_x$ acts both as the titanium source and conducting medium. This strategy simultaneously stabilizes the structure of MXene and obtains the NTO/Ti_3C_2 hybrids. The well-preserved 2D structure can effectively guarantee the larger electrode-electrolyte

---

* Corresponding authors.
E-mail addresses: mse_houlr@ujn.edu.cn (L. Hou), mse_yuancz@ujn.edu.cn, ayuancz@163.com (C. Yuan).

[1] Theses authors contributed equally to this work.

https://doi.org/10.1016/j.cclet.2020.02.016
1001-8417/

contacting area and facilitate the Na-ion migration. Meanwhile, the high conductivity originating from the Ti_3C_2 matrix leads to fast charge transmission. Moreover, the robust interface contact between NTO and Ti_3C_2 layer, and the excellent mechanical flexibility of Ti_3C_2 not only buffers the volume change during repeated charging/discharging but remits the peeling off of NTO, inhibiting the drop in capacity during cycling. Encouragingly, the NTO/Ti_3C_2 demonstrates large reversible capacities, excellent rate capability and ultralong lifespan, exhibiting fascinating potential in advanced SIBs.

The TiO_2/Ti_3C_2 hybrids were firstly prepared according to our previous work [25]. Then, 0.2 g of TiO_2/Ti_3C_2 powder was added in 40 mL of 10 mol/L NaOH solution. After sonication for 1 h, the mixture was poured into an autoclave (50 mL) and kept at 200 °C for 48 h. After washed with de-ionized (DI) water and dried under vacuum, the NTO/Ti_3C_2 hybrid was finally obtained.

Structures and morphologies of samples were investigated by X-ray powder diffraction (XRD, Rigaku Ultima IV, Japan), field-emission scanning electron microscopy (FESEM, JEOL-6300 F, 15 kV), transmission electron microscopy (TEM), scanning TEM (STEM), selected area electron diffraction (SAED) and high-resolution TEM (HRTEM) (JEOL JEM 2100 system) with an energy dispersive X-ray spectroscopy (EDS) system. The determination of surface elements was conducted by X-ray photoelectron spectroscopy (XPS, Thermo, Escalab 250xi) with Al K*a* monochromatic X-ray source ($h\nu$ =1486.6 eV). Raman spectrum was collected on Lab RAM HR Raman spectroscopy. The nitrogen adsorption/desorption isotherms were examined on NOVA 2000, Quantachrome.

The electrochemical performances of samples were tested on 2032 coin-type cells with the sodium metal foil as the counter/reference electrodes. The working electrodes slurry were prepared by mixing as-prepared active materials (70 wt%) with carbon black (20 wt%) and carboxymethyl cellulose (10 wt%) in DI water. Then, the slurry was pasting uniformly onto Copper foil substrate and dried at 110 °C for 11 h in vacuum. The glass fibers acted as the separator. 1.0 M $NaClO_4$ in a mixture of ethylene carbonate (EC)/propylene carbonate (PC) (1:1, v/v) with 5 wt% fluoroethylene carbonate (FEC) was used as the electrolyte. All cells were assembled in an argon-filled glove box (MBRAUN, Germany) with the concentrations of O_2 and $H_2O < 0.1$ ppm. Galvanostatic charge/discharge tests were conducted with the voltage range of 0.01–3.00 V (*vs.* Na/Na^+) by a LAND test system (Land CT2001A, China). The cyclic voltammetry (CV) tests in the potential range of 0.01–3.00 V were recorded by an electrochemical workstation (IviumStat.h, the Netherlands).

The whole synthetic strategy of layered NTO/Ti_3C_2 hybrid material is illustrated in Fig. 1a. Firstly, the Ti_3AlC_2 powder is etched fully by HF solution, forming the $Ti_3C_2T_x$ MXene. It is well known that the $Ti_3C_2T_x$ MXene tends to transform into stable oxide in dissolved oxygen under high temperatures due to the high portion of exposed Ti atoms on the surface. Accordingly, the TiO_2/Ti_3C_2 hybrid can be fabricated through a simple and friendly oxidation progress in DI water by hydration treatment. As a result, $Ti_3C_2T_x$ is partially oxidized, and Ti atoms on the surface of $Ti_3C_2T_x$ are *in-situ* transformed into TiO_2 nanoparticles (NPs). The NTO/Ti_3C_2 composite is further prepared by a hydrothermal alkalization process, in which the transformation of the TiO_2 NPs into the NTO nanoribbons occurs. Strikingly, the involved oxidation process we devised here is more moderate, and avoids the high-temperature annealing procedure during facile synthesis of the NTO. More importantly, the unique advantages of MXene itself can be greatly preserved in our case.

The structure of pure-phase $Ti_3C_2T_x$ and NTO/Ti_3C_2 composites (Fig. 1b) are characterized by typical XRD technique. Obviously, besides the signal (2θ = 7.2°) for the Ti_3C_2, those reflections centered at 14.6°, 22.9°, 29.9°, and 44.0° correspond to the (101), (110), (11-3), (12-4) planes of the $NaTi_8O_{13}$ (JCPDS No. 80-1284) with a space group R-3 (148), respectively, and the peaks centered at 40.7° and 60.6° are related to the (104) and (110) planes of the $NaTiO_2$ (JCPDS No. 89-0802) with space group R-3m (166), which indicates the co-existence of $NaTi_8O_{13}$ and $NaTiO_2$ phases in the resulted NTO/Ti_3C_2 specimen. Unexpectedly, the (11-3) peak of the $NaTi_8O_{13}$ has the highest diffraction intensity in XRD patterns. To be specific, the $NaTi_8O_{13}$ in the co-existence preferentially grows along the (11-3) plane. From this result, it is clear that the exists of the Ti_3C_2 matrix influences the driving force for $NaTi_8O_{13}$ growth, such as enhance the nucleation by creating disorder in the incorporation of adatoms into the lattice [28], thus induce a preferred growth in the (11-3) direction of the $NaTi_8O_{13}$. Notably, the characteristic (002) peak attributed to the $Ti_3C_2T_x$ shifts from $2\theta = 9.8°$ (the inset in Fig. 1b) to $2\theta = 7.2°$, suggesting the *d*-spacing value of the Ti_3C_2 matrix increases from 0.902 nm to 1.228 nm after the *in-situ* growth of the hexagonal NTO. All the above analyses confirm that the NTO phases have been successfully formed into the interlayers of the conductive Ti_3C_2 matrix.

Specific morphologies and micro-structures of the $Ti_3C_2T_x$, TiO_2/$Ti_3C_2T_x$ and NTO/Ti_3C_2 were characterized by FESEM and (HR) TEM measurements in detail. A panoramic view (Fig. 2a) reveals that the accordion-like multilayer feature of the $Ti_3C_2T_x$ obtained after acid etching from the bulk Ti_3AlC_2. Further closer examination (Fig. 2b) clearly shows the interlayer space of < 60 nm existing in the pristine $Ti_3C_2T_x$ with a smooth surface, which benefits more exposed electroactive sites. After the hydration process, the morphology becomes even rougher due to the *in-situ* formation

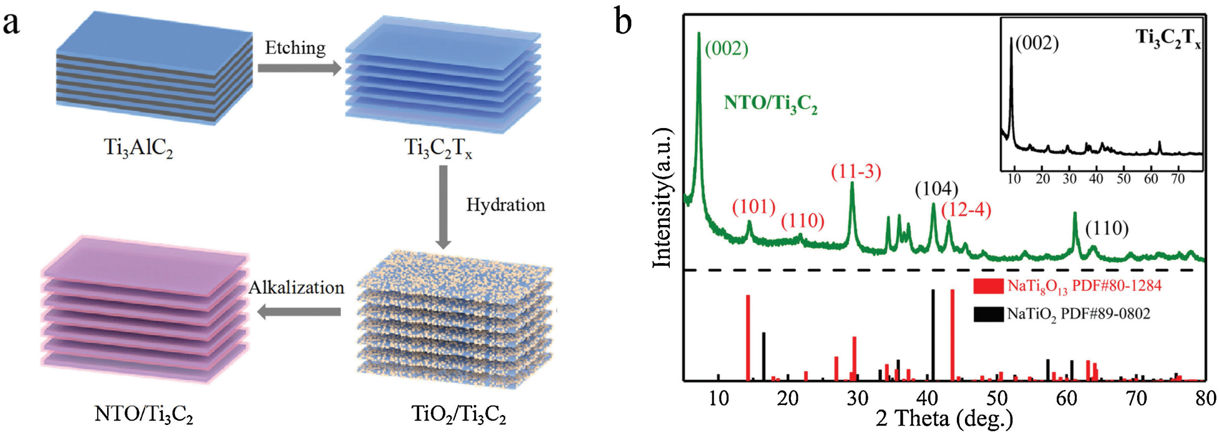

Fig. 1. (a) Schematic illustration for synthesizing the NTO/Ti_3C_2 composite. (b) XRD patterns of the NTO/Ti_3C_2 and $Ti_3C_2T_x$ (the upright inset in panel b).

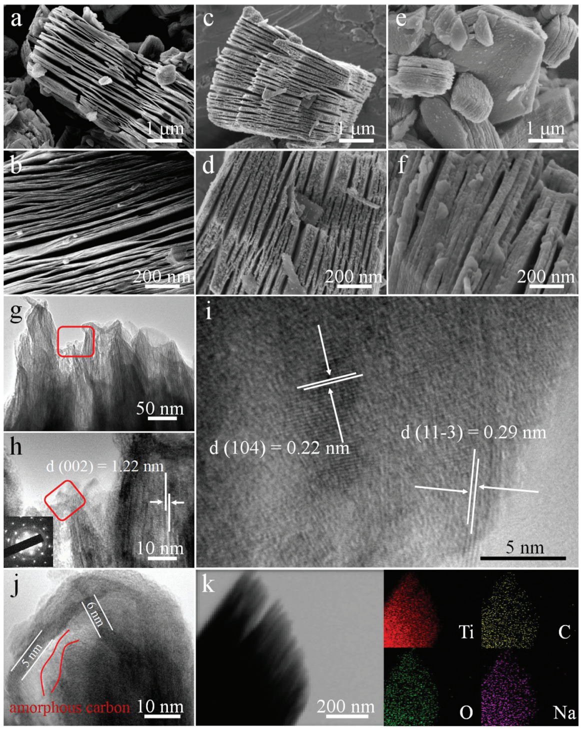

Fig. 2. FESEM images of (a, b) $Ti_3C_2T_x$, (c, d) TiO_2/Ti_3C_2 and (e, f) NTO/Ti_3C_2. (g-j) TEM/(HR)TEM, SAED pattern (the inset in panel h), (k) STEM and corresponding element (O, Sn and Ti) mapping images of the NTO/Ti_3C_2.

of TiO_2 NPs on the Ti_3C_2 surface (Figs. 2c and d). As shown in Figs. 2e and f, the anchored phases change from NPs to connected thin flats coating on the Ti_3C_2 NSs, suggesting the transformation of TiO_2 into the hybrid NTO after the following alkalization process. As we intended, both TiO_2/Ti_3C_2, and even NTO/Ti_3C_2 almost preserve the pristine 2D open structure, which reveals that the formation of NTO is under very mild condition, and do not cause the damage of intrinsic properties, *e.g.*, conductivity, intensity and ion transport characteristic, of the MXene.

The TEM image (Fig. 2g) clearly reveals the layered structure of NTO/Ti_3C_2 hybrids. The apparent lattice distance of 1.22 nm, as visualized in Fig. 2h, corresponds to the (002) crystalline plane of the Ti_3C_2 in the hybrid, which is in good line with the above XRD analysis. The dotted-line pattern in SAED (the inset in the Fig. 2h) manifests the crystalline structure of the hybrid. Under HRTEM observation (Fig. 2i), the lattice fringes are measured to be 0.22 nm and 0.29 nm, which are in good agreement with the (104) plane of the $NaTiO_2$ and (11-3) plane of the $NaTi_8O_{13}$, proving the successful *in-situ* growth of the NTO phases on the Ti_3C_2 surface. Expectedly, the *in-situ* formed NTO layer consists of well isolated elongated nanoribbons (Fig. 2j). Apparently, the NTO nanoribbons are about 5 nm in the thickness and interconnect with the Ti_3C_2 matrix through the disordered carbon “binder”. The perfect combination of the two components suppresses the volume change and peeling off of NTO under sodiation/desodiation process, and enhances the conductivity of the hybrid. The STEM image and corresponding elemental (Ti, C, O and Na) EDS mapping images (Fig. 2k) of the hybrid materials verify the uniform attachment of the NTO upon the Ti_3C_2 marix.

The chemical composition and surface valance state of the NTO/Ti_3C_2 are conducted by XPS analysis. The XPS survey spectrum (Fig. 3a) shows the co-existence of Al, C, Ti, O, F and Na elements in the hybrid material, in which the Na KLL (497 eV), F KLL (565/835 eV) and O KLL (976 eV) represent the Auger peaks for Na, F, K elements respectively [29]. The weak Al and F peaks, are derived from the raw material, and the fluorine functional groups on the surface of MXene due to the HF etching progress, respectively. The high resolution Ti 2p XPS spectrum (Fig. 3b) can be deconvolution into four pairs peaks, corresponding to Ti-C (455.3/461.1 eV), Ti^{2+} (456.6/462.8 eV), Ti^{3+} (458.3/464.1 eV) and Ti^{4+} (458.8/465.0 eV), respectively [26,27]. The large proportion of Ti-C peaks and low chemical state of Ti peaks indicate that the Ti_3C_2 matrix are well preserved after the oxidation and alkalization processes, which allows the merits of Ti_3C_2 to be fully utilized to enhance the electrochemical performance for sodium storage. Furthermore, the visual increasing Ti^{3+} and Ti^{4+} contribution, compared to the pristine MXene [25], reveals the successful formation of NTO in hybrid, along with the enhanced peak intense of elemental Na in the survey spectrum. The C 1s XPS spectrum of the hybrid (Fig. 3c) shows three kinds of C orbitals in NTO/Ti_3C_2, namely C-Ti (281.7 eV), C—C (284.8 eV, 288.7 eV), and C—O (286.1 eV), respectively [26]. The proportion of C—C peak increases obviously compared to pristine MXene [25], which can be attributed to carbon layers because of the precipitation of Ti atoms from Ti_3C_2 crystal during hydrothermal process. Further Raman observation of the NTO/Ti_3C_2 (Fig. S1 in Supporting information) shows the two broad peaks located at 1376.20 and 1595.93 cm^{-1}, which are associated with the disorderly induced characteristic D-band and the sp^2 hybridized graphitized G-band of carbon, respectively [30]. The ratio of D- and G- band intensity (I_D/I_G), is ~4.78, suggesting the appearance of disordered (amorphous) carbon layers in hybrid due to the precipitation and oxidation of the outermost Ti atoms in the MXene structure. Finally, the high-resolution O 1s spectrum (Fig. 3d) shows three components. Specifically, the main peak at 530.0 eV is attributed to the Ti—O bonds, and two broad peaks at the binding energy of 531.5 and 532.8 eV can be indexed well to the O—C and —OH groups, respectively [27].

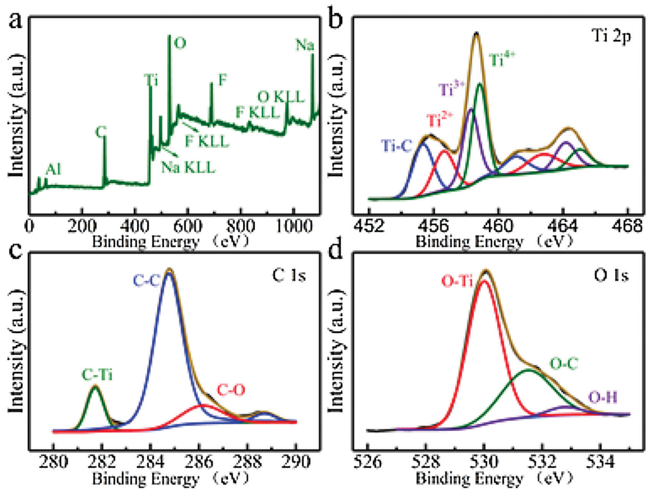

Fig. 3. XPS spectra of (a) survey spectrum, and high-resolution spectra of (b) Ti 2p, (c) C 1s and (d) O 1s for the NTO/Ti_3C_2 composite.

One advantage of this architecture is that the NTO forms not only on the surface of MXene sheets, but also in the layers of Ti_3C_2, as evidenced by XRD discussion above, which is also supported by the nitrogen sorption isotherms (Fig. S2 in Supporting information). Obviously, the isotherms of the $Ti_3C_2T_x$, TiO_2/Ti_3C_2 and NTO/Ti_3C_2 (Figs. S2a–c) exhibit typical-IV behaviors, indicating the main existence of mesopores in these samples. The Brunauer-Emmett-Teller (BET) surface area of the NTO/Ti_3C_2 is estimated as ~13.3 m^2/g, higher than those of $Ti_3C_2T_x$ (~9.5 m^2/g) and TiO_2/Ti_3C_2 (~11.6 m^2/g). The increased specific surface area for the hybrid benefits from the opening or swelling of the layers during oxidation and alkalization, which allows the adsorbates to penetrate between layers. Corresponding pore volume and average pore size (D) of the samples are calculated by using Barret-Joyner-Halenda (BJH) method (Table S1 in Supporting information). The D value of the NTO/Ti_3C_2 is ~9.8 nm, which is higher than those of $Ti_3C_2T_x$ (~9.0 nm) and TiO_2/Ti_3C_2 (~9.5 nm). The large pore size indicates the increased number of large mesopores in the hybrid NTO/Ti_3C_2, leading to the largest pore volume of ~0.045 cm^3/g for the NTO/Ti_3C_2, as collected in Table S1. The NTO/Ti_3C_2 hybrids with high BET surface area and porous structure could provide a large sur-/interfaces for the rapid penetration of electrolyte ions, hence achieving remarkably electrochemical sodium storage capacities.

Electrochemical properties of the NTO/Ti_3C_2 are firstly elucidated by cyclic voltammetry (CV) measurements. Fig. 4a shows the first three CV curves at a scan rate of 0.5 mV/s within a voltage window of 0.01–3.0 V *vs.* Na/Na^+. The cathodic curves exhibit great decay between the initial sweep and following scans, which arises from the irreversible formation of solid electrolyte interphase (SEI) layer between the electrode and electrolyte. Significantly, two pairs of peaks are observed in the subsequent cycles, located at 2.59/2.82 V and 2.50/2.73 V, which mainly attribute to the insertion/extraction of Na^+. It is worth noting that those cathodic and anodic peaks are almost overlapping in the second and third scanning cycles, demonstrating fairly high reversibility and stability of the NTO/Ti_3C_2 hybrid. Fig. 4b shows the first three discharge-charge curves of the NTO/Ti_3C_2 anode at a current density of 200 mAh/g. The initial discharge and charge capacity are ~162 and ~125 mAh/g respectively, corresponding to the initial Coulombic efficiency (ICE) of ~77.2%, which are higher than those of pristine $Ti_3C_2T_x$ in our previous work (~156 and ~77 mAh/g, corresponding to the ICE of ~59%) [25] due to the decrease of surface functional groups. It should be pointed out that the plateaus in discharge-charge curves correspond well with redox peaks in CV profiles. To evaluate the capacity and stability of the NTO/Ti_3C_2, the cycling properties of bare $Ti_3C_2T_x$, TiO_2/Ti_3C_2 and the NTO/Ti_3C_2 hybrids were comparatively conducted at 200 mAh/g for 500 consecutive cycles (Fig. 4c). A more attractive result is that the NTO/Ti_3C_2 anode has the highest specific capacity of ~118 mAh/g compared to the Ti_3C_2 (~75 mAh/g) and TiO_2/Ti_3C_2 (~101 mAh/g) after cycles. In addition, the NTO/Ti_3C_2 anode possesses the excellent rate performance with specific capacities of ~157, ~143, ~118, ~105, ~82 and ~78 mAh/g at 50, 100, 200, 500, 1000 and 2000 mA/g, respectively (Fig. 4d), which can be attributed to efficient ions and electrons transport in the electrode. Remarkably, when the current density is relaxed to 50 mA/g, the capacity can quickly returns to ~152 mAh/g. To fully prove the excellent stability of the NTO/Ti_3C_2 electrode, the high-rate cycling performance was tested (Fig. 4e), and impressively, the composite deliver a reversible capacity of 82 mAh/g at 2000 mA/g ever after 1900 cycles, exhibiting the preeminent stability of the hybrid anode.

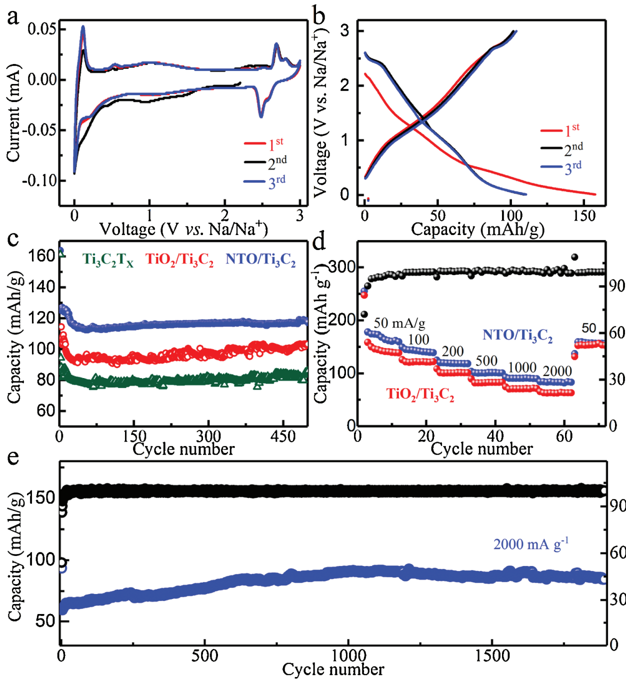

Fig. 4. (a) The 1st, 2nd and 3rd CV curves at 0.5 mV/s and (b) galvanostatic charge-discharge plots at 200 mA/g of NTO/Ti_3C_2 sample. (c) Cycle performance for all specimens at 200 mA/g. (d) Rate performance of the TiO_2/Ti_3C_2 and NTO/Ti_3C_2 anodes at various current densities ranging from 100 mA/g to 2000 mA/g, along with the CE data of the NTO/Ti_3C_2. (e) Long-term cycling performance and CE data of the NTO/Ti_3C_2 anode at 2000 mA/g.

In summary, a novel NTO/Ti_3C_2 hierarchical layered composite, in which the NTO nanoribbons *in-situ* growth on the surface of 2D Ti_3C_2 MXene, was successfully prepared by a mild two-step hydrothermal method. The well-preserved 2D structure, high conductivity originating from Ti_3C_2 matrix, and the synergistic effect between the NTO and the Ti_3C_2 hugely benefit to achievement of high-rate long cycle life and sodium-storage properties. Impressively, the NTO/Ti_3C_2 delivered a reversible and stable capacity of ~82 mAh/g even after 1900 cycles at 2000 mA/g for SIBs. More significantly, our investigation here provides a viable methodology to develop active and durable MXene-based hybrids for long-cycle-life SIBs in the near future.

Declaration of competing interest

The authors declare that they have no known competing financial interests or personal relationships that could have appeared to influence the work reported in this paper.

Acknowledgments

The authors acknowledge the financial support from National Natural Science Foundation of China (Nos. 51772127and 51772131), Taishan Scholars (No. ts201712050), Major Program of Shandong Province Natural Science Foundation (No. ZR2018ZB0317) and Collaborative Innovation Center of Technology and Equipment for Biological Diagnosis and Therapy in Universities of Shandong.

Appendix A. Supplementary data

Supplementary material related to this article can be found, in the online version, at doi:https://doi.org/10.1016/j.cclet.2020.02.016.

References

[1] J.M. Tarascon, M. Armand, Nature 414 (2001) 359–367.
[2] J. Liao, W. Ni, C. Wang, J. Ma, Chem. Eng. J. 391 (2020) 123489.
[3] Y. Liu, Z. Sun, K. Tan, et al., J. Mater. Chem. A 7 (2019) 4353–4382.
[4] B. Xu, S. Qi, M. Jin, et al., Chin. Chem. Lett. 30 (2019) 2053–2064.
[5] Y. Liu, Y. Fang, Z. Zhao, et al., Adv. Energy Mater. 9 (2019) 1970026.
[6] Q. Wang, S. Chu, S. Guo, Chin. Chem. Lett. (2019), doi:http://dx.doi.org/10.1016/j.cclet.2019.12.008.
[7] Y. Liu, F. Fan, J. Wang, et al., Nano Lett. 14 (2014) 3445–3452.
[8] Y. Gogotsi, ACS Nano 8 (2014) 5369–5371.
[9] Y. Jiang, M. Hu, D. Zhang, et al., Nano Energy 5 (2014) 60–66.
[10] X. Xiong, C. Yang, G. Wang, et al., Energy Environ. Sci. 10 (2017) 1757–1763.
[11] Y. Cao, L. Xiao, M.L. Sushko, et al., Nano Lett. 12 (2012) 3783–3787.
[12] Z. Yan, Q.W. Yang, Q. Wang, J. Ma, Chin. Chem. Lett. 31 (2020) 583–588.
[13] N. Wang, Z. Bai, Y. Qian, J. Yang, Adv. Mater. 28 (2016) 4126–4133.
[14] J. Qian, X. Wu, Y. Cao, X. Ai, H. Yang, Angew. Chem. Int. Ed. 52 (2013) 4633–4636.
[15] Z. Yan, L. Liu, H. Shu, et al., J. Power Sources 274 (2015) 8–14.
[16] X. Wang, Y. Li, Y. Gao, Z. Wan, L. Chen, Nano Energy 13 (2015) 687–692.
[17] L. Que, F. Yu, L. Zheng, Z.-B. Wang, D. Gu, Nano Energy 45 (2018) 337–345.

[18] L.-Y. Liu, Y. Ding, B. Zhou, et al., Appl. Sci. 9 (2019) 1673.
[19] Y. Zhang, L. Guo, S. Yang, Nanoscale 7 (2015) 14618–14626.
[20] A. Rudola, K. Saravanan, S. Devaraj, H. Gong, P. Balaya, Chem. Commun. 49 (2013) 7451–7453.
[21] Y. Dong, Z.S. Wu, S. Zheng, et al., ACS Nano 11 (2017) 4792–4800.
[22] B. Xu, S. Qi, M. Jin, et al., Chin. Chem. Lett. 30 (2019) 2053–2064.
[23] D. Xiong, X. Li, Z. Bai, S. Lu, Small 14 (2018) 1703419.
[24] M. Xu, N. Bai, H.-X. Li, et al., Chin. Chem. Lett. 29 (2018) 1313–1316.
[25] C. Yang, Y. Liu, X. Sun, et al., Electrochim. Acta 271 (2018) 165–172.
[26] J. Halim, K.M. Cook, M. Naguib, et al., Appl. Surf. Sci. 362 (2016) 406–417.
[27] S. Niu, Z. Wang, M. Yu, et al., ACS Nano 12 (2018) 3928–3937.
[28] B. Yang, P. Zhang, G. Wang, et al., Coatings 9 (2019) 758.
[29] E. Adem, VG Scientific XPS Handbook, VG Scientific Limited, West Sussex, 1991, pp. 3–30.
[30] A.C. Ferrari, J. Meyer, V. Scardaci, et al., Phys. Rev. Lett. 97 (2006) 187401.